

Higher-Order Topology in Monolayer FeSe

Gan Zhao,¹ Haimen Mu,¹ Huimin Zhang,² and Z. F. Wang^{1,*}

¹*Hefei National Laboratory for Physical Sciences at the Microscale,
CAS Key Laboratory of Strongly-Coupled Quantum Matter Physics, Department of Physics,
University of Science and Technology of China, Hefei, Anhui 230026, China*

²*Department of Physics and Astronomy,
West Virginia University, Morgantown, WV, 26506, USA*

Abstract

Generally, the topological corner state in two-dimensional second-order topological insulator (2D SOTI) is equivalent to the well-known domain wall state, originated from the mass-inversion between two adjacent edges with phase shift of π . In this work, go beyond this conventional physical picture, we report a fractional mass-kink induced 2D SOTI in monolayer FeSe with canted checkerboard antiferromagnetic (AFM) order by analytic model and first-principles calculations. The canted spin associated in-plane Zeeman field can gap out the quantum spin Hall edge state of FeSe, forming a fractional mass-kink with phase shift of $\pi/2$ at the rectangular corner, and generating an in-gap topological corner state with fractional charge of $e/4$. Moreover, the topological corner state is robust to local perturbation, existing in both naturally and non-naturally cleaved corners, regardless of the edge orientation. Our results not only demonstrate a material system to realize the unique 2D AFM SOTI, but also pave a new way to design the higher-order topological states from fractional mass-kink with arbitrary phase shift, which are expected to draw immediate experimental attention.

Keywords: Monolayer FeSe, antiferromagnetic second-order topological insulator, fractional mass-kink

*E-mail: zfwang15@ustc.edu.cn

INTRODUCTION

With the rapid progress in classification of topological electronic states [1, 2], different kinds of topological materials are predicted theoretically and confirmed experimentally [3–5]. However, the prior studies are mainly focused on the first-order topological materials [6–8], where the topological boundary state only appears at dimension one lower than that of the bulk state. When this conventional bulk boundary correspondence is extended to the higher-order form [9], a new class of topological materials called higher-order topological insulator emerges [10–13]. The m -dimensional n th-order topological insulator holds gapless state at $(m-n)$ -dimensional boundary but gapped state otherwise. Therefore, the two-dimensional second-order topological insulator (2D SOTI) is characterized by gapped topological edge state and in-gap topological corner state. Different to symmetry protected bulk topological index, physically, the emergence of in-gap topological corner state can also be understood by the well-known mass-inversion mechanism in Jackiw-Rebbi model [14], which can support a localized domain wall state, as shown schematically in Fig. 1(a).

Currently, although a variety of theoretical models are proposed for the 2D SOTI [15–29], its material realization is still a challenging task. Besides some artificial macro-structures [30–36], few realistic electronic materials have been reported. What’s more, the limited 2D SOTI materials, such as graphdiyne [37, 38], γ -graphyne [39] and twisted-bilayer graphene [40–42], are all describable by the mass-inversion mechanism. Recently, this physical mechanism is extended to a more universal form for generating the domain wall state [43], as shown schematically in Fig. 1(b). The mass distribution along the edge is characterized by the mass-angle, which is θ and $\theta + \Delta\theta$ for left- and right-part, respectively. Based on model calculations, the localized domain wall state is achieved in this fractional mass-kink [44] with any non-zero phase shift ($\Delta\theta \neq 0$). Obviously, the mass-inversion in Fig. 1(a) just corresponds to one special case of $\Delta\theta = \pi$ in Fig. 1(b). The fractional mass-kink further lowers the physical requirement to realize the domain wall state, providing much freedom to design the 2D SOTI. However, no material systems are reported for this peculiar non- π phase shift associated topological corner state, greatly hindering the experimental verification.

Due to the tunable topological phase transition between first- and higher-order topological states [45, 46], the quantum spin Hall (QSH) materials provide a good platform to explore the 2D SOTI. As the parent compound of Fe-based superconductor, the monolayer FeSe has been intensively studied [47]. Recently, the QSH state with checkerboard antiferromagnetic (AFM) order (Fig. 1(c)) is confirmed experimentally in monolayer FeSe [48], demonstrating an exotic topological phase in this high-temperature superconductor [49, 50]. In this work,

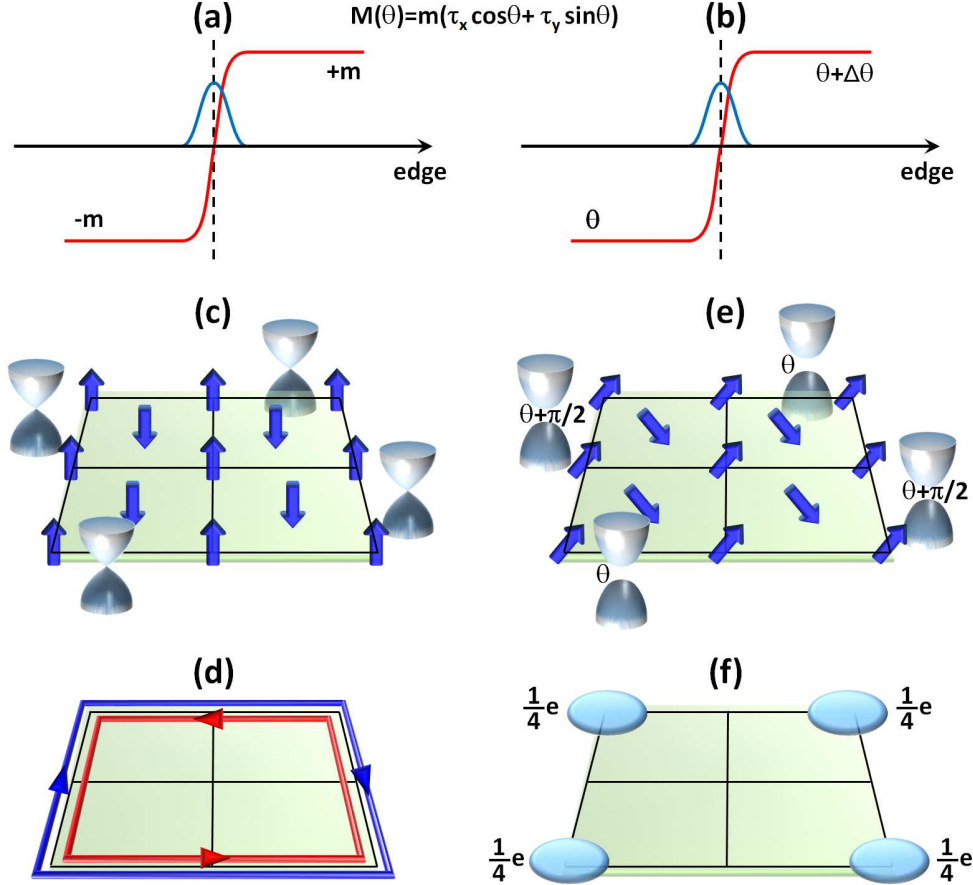


Figure 1: Schematic mass distribution along the edge (red line) and localized domain wall state (blue line) for (a) mass-inversion, (b) fractional mass-kink. The mass M is defined in edge state space, m is mass-intensity, θ is mass-angle, $\Delta\theta$ is phase shift across the domain wall, τ_x and τ_y are Pauli matrix of the edge state. (c) Schematic checkerboard AFM order in monolayer FeSe and gapless topological edge state. (d) Schematic real-space distribution of gapless topological edge state (QSH edge state), showing the propagating direction (arrow) and spin (red and blue color). (e) Schematic canted checkerboard AFM order in monolayer FeSe and gapped topological edge state. The adjacent edges have a different mass-angle of θ and $\theta + \pi/2$. (f) Schematic real-space distribution of in-gap topological corner state, holding a fractional charge of $e/4$.

starting from the AFM QSH state, we report a 2D SOTI in monolayer FeSe with canted checkerboard AFM order (Fig. 1(e)). An intriguing fractional mass-kink induced topological corner state is identified by analytic model and first-principles calculations, which is robust to local perturbation and edge orientation. The main discoveries of our work are summarized in Fig. 1. Since the AFM QSH state has a pair of helical Dirac edge states (Fig. 1(c) and 1(d)), the coupling between them will break the band degeneracy at the Dirac point. Physically,

this can be achieved by the canted spin induced in-plane Zeeman field. Meanwhile, the fractional mass-kink with phase shift of $\pi/2$ is formed at the rectangular corner (Fig. 1(e)), resulting in an in-gap topological corner state with fractional charge of $e/4$ (Fig. 1(f)).

RESULTS

The nontrivial band topology of monolayer FeSe with checkerboard AFM order is captured by its band structures around M point in the first Brillouin zone [48]. The low-energy effective Hamiltonian derived from the first-principle calculations is written as [51]

$$H = a_0(k_x^2 + k_y^2)s_0\sigma_0 + a_1k_xk_ys_0\sigma_x + \lambda s_z\sigma_y + a_2(k_x^2 - k_y^2)s_0\sigma_z \quad (1)$$

where σ_0 and s_0 are identity matrix, $\sigma_{x,y,z}$ is orbital Pauli matrix, s_z is spin Pauli matrix, $a_{0,1,2}$ is fitting constant, and λ is intrinsic spin-orbital coupling (SOC). The characterized band structures of Eq. (1) are shown in Fig. 2, exhibiting a fourfold rotational symmetry ($C_4 = i\sigma_y e^{i\pi s_z/4}$). Without SOC, there is a quadratic band degeneracy at M point (Fig. 2(a)). With SOC, the degeneracy is lift and an AFM QSH state is realized (Fig. 2(b)). One can see that this effective Hamiltonian is dramatically different to Kane-Mele [52] and Bernevig-Hughes-Zhang [53] model described QSH state that includes the linear term of momentum. The helical Dirac edge state for such a quadratic QSH Hamiltonian [54–56] has not been analytically derived yet.

The first term in Eq. (1) is a reference energy that doesn't affect our final results, so we omit it in the following part. To simplify the derivation of the helical Dirac edge state along different edges, we define a rotated coordinate system k_1 - k_2 , where the edge along k_2 direction has an angle φ with k_x axis, as shown in Fig. 2(c). For the rectangular cluster with 90° corners, the four regular edges are along the direction of $\varphi = 0, \pi/2, \pi$ and $3\pi/2$, as shown in Fig. 2(d). In the k_1 - k_2 plane, Eq. (1) can be rewritten as

$$H_{\pm} = \mp a_1k_1k_2s_0\sigma_x + \lambda s_z\sigma_y \pm a_2(k_2^2 - k_1^2)s_0\sigma_z \quad (2)$$

where H_+ for $\varphi=0, \pi$ and H_- for $\varphi=\pi/2, 3\pi/2$. Assuming Eq. (2) is defined in half-space ($k_1>0$) of the k_1 - k_2 plane, we replace $k_1 \rightarrow -i\partial_{x_1}$, $k_2 \rightarrow 0$, and substitute a trial edge state solution $\psi = e^{\eta x_1}\phi$ into it, where η is a decay constant. Then, Eq. (2) is reduced to the form

$$\tilde{H}_{\pm} = \lambda s_z\sigma_y \pm a_2\eta^2s_0\sigma_z \quad (3)$$

The spin is decoupled in this bulk Hamiltonian, so the edge state solution will also be spin-decoupled, which has a form of $|\psi_{\uparrow\pm}\rangle = (|\phi_{\uparrow\pm}\rangle, 0)^T$ and $|\psi_{\downarrow\pm}\rangle = (0, |\phi_{\downarrow\pm}\rangle)^T$. Substituting

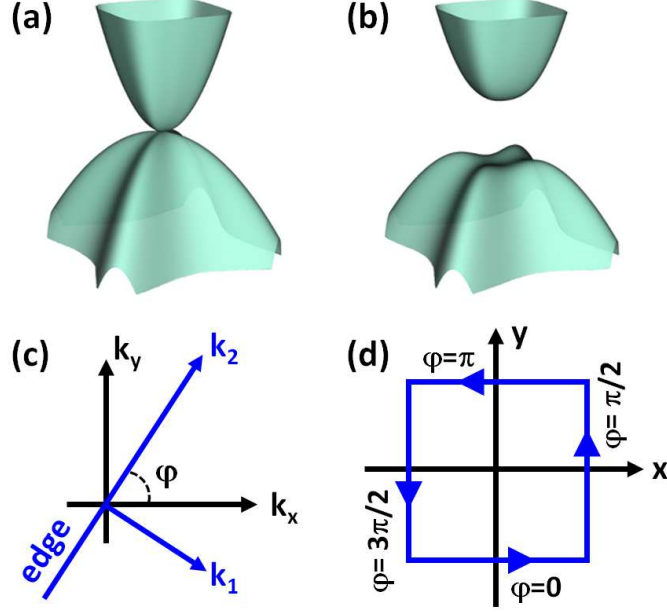


Figure 2: (a) and (b) Characterized band structures of the low-energy effective Hamiltonian without and with SOC, showing the quadratic touching point and quadratic QSH. (c) Reciprocal space rotated coordinate system for describing the edge along k_2 direction that has a angle φ with k_x axis. (d) Real space rectangular cluster with four edges, corresponding to $\varphi = 0, \pi/2, \pi$ and $3\pi/2$ in (c). The arrow denotes the positive direction of the edge.

$|\psi_{\uparrow+}\rangle$ and $|\psi_{\downarrow+}\rangle$ into \tilde{H}_+ , considering the solution divergence ($x_1 \rightarrow +\infty$) and time-reversal symmetry ($T = is_y K$, K is Hermitian conjugate), we obtain the edge state solution of \tilde{H}_+ as

$$\begin{aligned} |\phi_{\uparrow+}\rangle &= \alpha e^{\eta x_1} |\xi_+\rangle + \beta e^{\eta^* x_1} |\xi_-\rangle \\ |\phi_{\downarrow+}\rangle &= -|\phi_{\uparrow+}^*\rangle \end{aligned} \quad (4)$$

where $\eta^2 = i\lambda/a_2$, α and β are coefficients, and $|\xi_{\pm}\rangle = \sqrt{2}/2(1, \pm 1)^T$ are eigenstate of σ_x . Since \tilde{H}_{\pm} are connected by the C_4 symmetry, that is $\tilde{H}_- = C_4^{-1} \tilde{H}_+ C_4$, the edge state solution of \tilde{H}_- can be obtained from the relation

$$\begin{aligned} |\psi_{\uparrow-}\rangle &= C_4^{-1} |\psi_{\uparrow+}\rangle \\ |\psi_{\downarrow-}\rangle &= C_4^{-1} |\psi_{\downarrow+}\rangle \end{aligned} \quad (5)$$

In the edge state space ($|\psi_{\uparrow\pm}\rangle, |\psi_{\downarrow\pm}\rangle$), to the leading order of k_2 , Eq. (2) can be transformed into the standard Dirac equation as

$$h_{\pm} = a_1 k_2 \text{Im}(\eta) \tau_z \quad (6)$$

where τ_z is Pauli matrix of the edge state, showing a general form of the helical Dirac edge state for the quadratic QSH Hamiltonian.

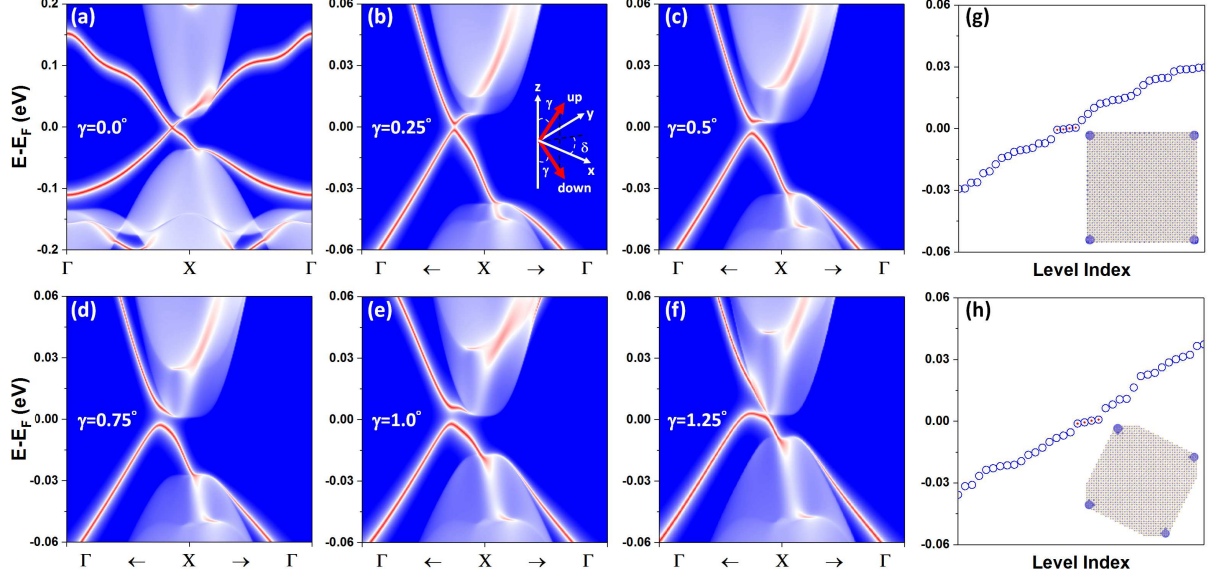


Figure 3: (a) The gapless QSH edge state along ferromagnetic edge of monolayer FeSe with checkerboard AFM order. (b-f) Zoom-in gapped topological edge state by canting the spin direction with $\delta = 45^\circ$, (b) $\gamma = 0.25^\circ$, (c) $\gamma = 0.5^\circ$, (d) $\gamma = 0.75^\circ$, (e) $\gamma = 1.0^\circ$ and (f) $\gamma = 1.25^\circ$. The canted spin-up and -down directions are determined by angle γ and δ , as shown schematically in inset of (b). (g) Discrete energy levels of rectangular monolayer FeSe cluster with four naturally cleaved ferromagnetic edges of the same spin. The four in-gap topological corner states are marked in red-dot around the Fermi-level. The inset is spatial charge density distribution of the corner states. The radii of circle on each atom denotes the absolute value of charge density. (h) is the same as (g), but for a rotated rectangular cluster with non-naturally cleaved ferromagnetic edges of the same spin.

In order to gap out the helical Dirac edge state in Eq. (6), we consider an in-plane Zeeman field as [45]

$$H' = us_x\sigma_0 + vs_y\sigma_0 \quad (7)$$

where $s_{x,y}$ is spin Pauli matrix, u and v are coefficients that control the intensity and direction of in-plane Zeeman field. This new term breaks the spin-degeneracy and mixes the spin-up and -down in Eq. (1). Similar to the above derivation, Eq. (7) can be written in the edge state space as [43]

$$\begin{aligned} h'_+ &= m(\tau_x \cos\theta + \tau_y \sin\theta) \\ h'_- &= m[\tau_x \cos(\theta + \pi/2) + \tau_y \sin(\theta + \pi/2)] \end{aligned} \quad (8)$$

where h'_+ for $\varphi = 0, \pi$ and h'_- for $\varphi = \pi/2, 3\pi/2$. $\tau_{x,y}$ is Pauli matrix of the edge state, $m_1 = \text{Re}(\frac{\alpha^2}{2\eta} + \frac{\beta^2}{2\eta^*})$, $m_2 = \text{Im}(\frac{\alpha^2}{2\eta} + \frac{\beta^2}{2\eta^*})$, $m = [(u^2 + v^2)(m_1^2 + m_2^2)]^{1/2}$, $m \cos\theta = um_1 - vm_2$

and $m\sin\theta = um_2 + vm_1$. Combining Eq. (6) and Eq. (8), the helical Dirac edge state is gapped out with a band gap of $E_g = 2m$. If the intensity of in-plane Zeeman field $(u^2 + v^2)^{1/2}$ is fixed, the Dirac gap will independent of the direction of in-plane Zeeman field and mass-angle. Most remarkably, one notices that the mass-angle is θ and $\theta + \pi/2$ for edge along $\varphi = 0, \pi$ and $\varphi = \pi/2, 3\pi/2$, respectively, forming a fractional mass-kink with phase shift of $\Delta\theta = \pi/2$ at each 90° corner. According to Moore's theory [43], such a phase shift will support a topological corner state with fractional charge of $N_s = e|\Delta\theta/2\pi| = e/4$. Therefore, a 2D SOTI is identified in the monolayer FeSe, originated from the in-plane Zeeman field induced fractional mass-kink with non- π phase shift. More details about the analytic derivations can be found in the Supplementary Data.

To further support our analytic results, the first-principles calculations are performed to directly identify the unique gapped topological edge state and in-gap topological corner state in monolayer FeSe. The gapless QSH edge state along ferromagnetic edge of [100] direction for monolayer FeSe with checkerboard AFM order is shown in Fig. 3(a), where the PT symmetry protected Dirac point is sitting along Γ -X direction [48]. In order to introduce an in-plane Zeeman field to gap out the topological edge state, a special canted checkerboard AFM order is considered (Fig. 1(e)) [57]. The direction of canted spin is determined by zenith angle (γ) and azimuth angle (δ), as shown schematically in inset of Fig. 3(b). Experimentally, this spin configuration can be realized by applying an in-plane magnetic field, making the spin canted along the field direction, where zenith and azimuth angle is tunable by the field intensity and direction [58]. Interestingly, we found that the spectra of topological edge state with canted spin is insensitive to δ (see Fig. S1), that is, it doesn't depend on the direction of in-plane Zeeman field, which is consistent with our analytic derivation. Without losing the generality, we will fix δ and discuss the effect of γ in the following part. For azimuth angle $\delta = 45^\circ$ along [110] direction, the zoom-in topological edge state with small zenith angle ranging from $\gamma = 0.25^\circ$ to 1.25° is shown in Fig. 3(b) to 3(f), respectively. Comparing to the gapless spectra shown in Fig. 3(a), there are two significant features can be observed for the canted spin. First, the spin-degenerate bulk bands are split and bulk gap around X point is reduced with the increasing of γ . This feature can be attributed to the in-plane Zeeman field induced spin-splitting that results in upshift and downshift of the opposite spin bands (see Fig. S2). With the increasing of γ , the intensity of in-plane Zeeman field is enhanced, so the band splitting is increased and bulk gap between opposite spins is reduced. Second, the topological edge state is gapped out and Dirac gap exhibits a non-monotonic behavior with the increasing of γ . This feature can be attributed to the in-plane Zeeman field induced mass-

term and band-reshaping. According to our analytic results, the Dirac gap is proportional to the intensity of in-plane Zeeman field. In principles, it will increase with the increasing of γ . However, the reduced bulk gap moves the bottom branch of topological edge state gradually close to the top bulk band, making the global Dirac gap decreased with further increasing of γ . Therefore, based on canted checkerboard AFM order, we confirm the gapped topological edge state in monolayer FeSe, identifying the first unique character of 2D SOTI.

Since the band topology is same in the canted spin opened Dirac gap, we will focus on one gapped topological edge state with $\gamma = 0.75^\circ$ and $\delta = 45^\circ$ (Fig. 3(d)) to illustrate its corner state (see Fig. S3(a)-(c)). The rectangular cluster with 90° corners is constructed by cutting four ferromagnetic edges with the same spin along naturally cleaved [100] and [010] directions [59]. The discrete energy levels of the cluster are shown in Fig. 3(g). Clearly, there are four nearly degenerate corner states around the Fermi-level, as labeled by the red-dot. The spatial distribution of them is shown in the inset of Fig. 3(g), which is localized at four corners. Therefore, we confirm the in-gap topological edge state in monolayer FeSe, identifying the second unique character of 2D SOTI. Furthermore, by accounting the total electrons in the system [37], there is only one electron is left after filling all energy levels below the four corner states. Consequently, each corner state will hold a fractional charge of $e/4$, which is consistent with our analytic derivation.

In order to facilitate the possible experimental measurement, the robustness of topological corner state against the disorder and edge-cutting orientation are further investigated. The local disorder is simulated by adding finite random on-site energy to atoms around the corner. There are still four corner states localized at the corners, but the relative intensity is different between the corner with and without disorder (see Fig. S3(d)). Most importantly, we found that the rectangular cluster constructed from non-naturally cleaved ferromagnetic edge along arbitrary orientations can also support the existence of topological corner state. The discrete energy levels and spatial distribution of the corner states are shown in Fig. 3(h) and its inset, which are comparable to those shown in Fig. 3(g) and its inset. Moreover, the same results are obtained for the rectangular cluster with four antiferromagnetic edges (see Fig. S3(e)). Consequently, the topological corner state in monolayer FeSe can be revealed by cutting the edge along irregular orientation, providing more convenience for scanning tunneling microscopy detection. Additionally, if monolayer FeSe is stacked vertically into a three-dimensional (3D) structure of (LiFe)OHFeSe [60], the angle-resolved photoemission spectroscopy measured band structures [61] are similar to the monolayer FeSe studied in this work [48]. Considering the weak coupling between the neighboring FeSe layers in

(LiFe)OHFeSe [62], a 3D weak SOTI [63] is also realizable by the canted checkerboard AFM order, where the topological corner state is stacked into a one-dimensional topological hinge state with little dispersion along the vertical direction, supporting a quantized hinge conductance (see Fig. S4).

CONCLUSION

In conclusion, based on analytic model and first-principles calculations, we identify an intriguing fractional mass-kink induced topological corner state in monolayer FeSe with canted checkerboard AFM order. Our results greatly extend the topological physics for mass-inversion induced domain wall state and provide a new way to design the higher-order topological materials. The coupling between topological corner state and superconducting state in monolayer FeSe will also offer an attractive opportunity to realize the majorana fermion in the future.

FUNDING

This work was supported by NSFC (Grant No. 11774325 and 21603210), National Key Research and Development Program of China (Grant No. 2017YFA0204904) and Fundamental Research Funds for the Central Universities. We also thank Supercomputing Center at USTC for providing the computing resources.

-
- [1] Chiu CK, Teo JC and Schnyder AP *et al.* Classification of topological quantum matter with symmetries. *Rev Mod Phys* 2016; **88**: 035005.
- [2] Po HC, Vishwanath A and Watanabe H. Symmetry-based indicators of band topology in the 230 space groups. *Nat Commun* 2017; **8**: 1-9.
- [3] Hasan MZ and Kane CL. Colloquium: topological insulators. *Rev Mod Phys* 2010; **82**: 3045.
- [4] Bansil A, Lin H and Das T. Colloquium: Topological band theory. *Rev Mod Phys* 2016; **88**: 021004.
- [5] Liu P, Williams JR and Cha JJ. Topological nanomaterials. *Nat Rev Mater* 2019; **4**: 479-496.
- [6] Tang F, Po HC and Vishwanath A *et al.* Comprehensive search for topological materials using symmetry indicators. *Nature* 2019; **566**, 486-489.
- [7] Zhang T, Jiang Y and Song Z *et al.* Catalogue of topological electronic materials. *Nature* 2019; **566**: 475-479.
- [8] Vergniory M, Elcoro L and Felser C *et al.* A complete catalogue of high-quality topological materials. *Nature* 2019; **566**: 480-485.
- [9] Benalcazar WA, Bernevig BA and Hughes TL. Electric multipole moments, topological multipole moment pumping, and chiral hinge states in crystalline insulators. *Phys Rev B* 2017; **96**: 245115.
- [10] Benalcazar WA, Bernevig BA and Hughes TL. Quantized electric multipole insulators. *Science* 2017; **357**: 61-66.
- [11] Song Z, Fang Z and Fang C. (d-2)-dimensional edge states of rotation symmetry protected topological states. *Phys Rev Lett* 2017; **119**: 246402.
- [12] Schindler F, Cook AM and Vergniory MG *et al.* Higher-order topological insulators. *Sci Adv* 2018; **4**: eaat0346.
- [13] Langbehn J, Peng Y and Trifunovic L *et al.* Reflection-symmetric second-order topological insulators and superconductors. *Phys Rev Lett* 2017; **119**: 246401.
- [14] Jackiw R and Rebbi C. Solitons with fermion number 1/2. *Phys Rev D* 1976; **13**: 3398.
- [15] Ezawa M. Higher-order topological insulators and semimetals on the breathing kagome and pyrochlore lattices. *Phys Rev Lett* 2018; **120**: 026801.
- [16] Yan Z, Song F and Wang Z. Majorana corner modes in a high-temperature platform. *Phys Rev Lett* 2018; **121**: 096803.
- [17] Wang Q, Liu CC and Lu YM *et al.* High-temperature majorana corner states. *Phys Rev Lett* 2018; **121**: 186801.

- [18] Benalcazar WA, Li T and Hughes TL. Quantization of fractional corner charge in C_n -symmetric higher-order topological crystalline insulators. *Phys Rev B* 2019; **99**: 245151.
- [19] Liu F, Deng HY and Wakabayashi K. Helical topological edge states in a quadrupole phase. *Phys Rev Lett* 2019; **122**: 086804.
- [20] Zou J, He Z and Xu G. Higher-order topological insulators in a crisscross antiferromagnetic model. *Phys Rev B* 2019; **100**, 235137.
- [21] Liu T, Zhang YR and Ai Q *et al.* Second-order topological phases in non-hermitian systems. *Phys Rev Lett* 2019; **122**: 076801.
- [22] Yang Y, Jia Z and Wu Y *et al.* Gapped topological kink states and topological corner states in honeycomb lattice. *Sci Bull* 2020; **65**: 531-537.
- [23] Wakao H, Yoshida T and Araki H *et al.* Higher-order topological phases in a spring-mass model on a breathing kagome lattice. *Phys Rev B* 2020; **101**: 094107.
- [24] Ren Y, Qiao Z and Niu Q. Engineering corner states from two-dimensional topological insulators. *Phys Rev Lett* 2020; **124**: 166804.
- [25] Chen C, Song Z and Zhao JZ *et al.* Universal approach to magnetic second-order topological insulator. *Phys Rev Lett* 2020; **125**: 056402.
- [26] Chen R, Chen CZ and Gao JH *et al.* Higher-order topological insulators in quasicrystals. *Phys Rev Lett* 2020; **124**: 036803.
- [27] Yang YB, Li K and Duan LM *et al.* Higher-order topological anderson insulators. *Phys Rev B* 2021; **103**: 085408.
- [28] Agarwala A, Juričić V and Roy B. Higher-order topological insulators in amorphous solids. *Phys Rev Res* 2020; **2**: 012067.
- [29] Wu YJ, Hou J and Li YM *et al.* In-plane zeeman-field-induced majorana corner and hinge modes in an s-wave superconductor heterostructure. *Phys Rev Lett* 2020; **124**: 227001.
- [30] Peterson CW, Benalcazar WA and Hughes TL *et al.* A quantized microwave quadrupole insulator with topologically protected corner states. *Nature* 2018; **555**: 346-350.
- [31] Noh J, Benalcazar WA, Huang S *et al.* Topological protection of photonic mid-gap defect modes. *Nat Photon* 2018; **12**: 408-415.
- [32] Xue H, Yang Y and Gao F *et al.* Acoustic higher-order topological insulator on a kagome lattice. *Nat Mater* 2019; **18**: 108-112.
- [33] Ni X, Weiner M and Alu A *et al.* Observation of higher-order topological acoustic states protected by generalized chiral symmetry. *Nat Mater* 2019; **18**: 113-120.
- [34] Fan H, Xia B and Tong L *et al.* Elastic higher-order topological insulator with topologically

- protected corner states. *Phys Rev Lett* 2019; **122**: 204301.
- [35] Xie BY, Su GX and Wang HF *et al.* Visualization of higher-order topological insulating phases in two-dimensional dielectric photonic crystals. *Phys Rev Lett* 2019; **122**: 233903.
- [36] Zhang X, Wang HX and Lin ZK *et al.* Second-order topology and multidimensional topological transitions in sonic crystals. *Nat Phys* 2019; **15**: 582-588.
- [37] Lee E, Kim R and Ahn J *et al.* Two-dimensional higher-order topology in monolayer graphdiyne. *npj Quantum Materials* 2020; **5**: 1-7.
- [38] Sheng XL, Chen C and Liu H *et al.* Two-dimensional second-order topological insulator in graphdiyne. *Phys Rev Lett* 2019; **123**: 256402.
- [39] Liu B, Zhao G and Liu Z *et al.* Two-dimensional quadrupole topological insulator in γ -graphyne. *Nano Lett* 2019; **19**: 6492-6497.
- [40] Park MJ, Kim Y and Cho GY *et al.* Higher-order topological insulator in twisted bilayer graphene. *Phys Rev Lett* 2019; **123**: 216803.
- [41] Ma C, Wang Q and Mills S *et al.* Moiré band topology in twisted bilayer graphene. *Nano Lett* 2020; **20**: 6076-6083.
- [42] Liu B, Xian L and Mu H *et al.* Higher-order band topology in twisted moiré superlattice. *Phys Rev Lett* 2021; **126**: 066401.
- [43] Wang YQ and Moore JE. Boundary edge networks induced by bulk topology. *Phys Rev B* 2019; **99**: 155102.
- [44] Spurrier S and Cooper NR. Kane-Mele with a twist: Quasicrystalline higher-order topological insulators with fractional mass kinks. *Phys Rev Res* 2020; **2**: 033071.
- [45] Ezawa M. Topological switch between second-order topological insulators and topological crystalline insulators. *Phys Rev Lett* 2018; **121**: 116801.
- [46] Ezawa M. Magnetic second-order topological insulators and semimetals. *Phys Rev B* 2018; **97**: 155305.
- [47] Huang D and Hoffman JE. Monolayer FeSe on SrTiO₃. *Ann Rev Condens Matter Phys* 2017; **8**: 311-336.
- [48] Wang ZF, Zhang H and Liu D *et al.* Topological edge states in a high-temperature superconductor FeSe/SrTiO₃ (001) film. *Nat Mater* 2016; **15**: 968-973.
- [49] Hao N and Hu J. Topological quantum states of matter in iron-based superconductors: from concept to material realization. *Natl Sci Rev* 2019; **6**: 213-226.
- [50] Qiao S, Zhang P and Ding H *et al.* Fingerprint of checkerboard antiferromagnetic order in FeSe monolayer due to magnetic-electric correlation. *Mater Today* 2020; **41**: 44-50.

- [51] Wang ZF, Liu Z and Yang J *et al.* Light-induced type-II band inversion and quantum anomalous hall state in monolayer FeSe. *Phys Rev Lett* 2018; **120**: 156406.
- [52] Kane CL and Mele EJ. Quantum spin Hall effect in graphene. *Phys Rev Lett* 2005; **95**: 226801.
- [53] Bernevig BA, Hughes TL and Zhang SC. Quantum spin Hall effect and topological phase transition in HgTe quantum wells. *Science* 2006; **314**: 1757-1761.
- [54] Si C, Jin KH and Zhou J *et al.* Large-gap quantum spin Hall state in MXenes: d-band topological order in a triangular lattice. *Nano Lett* 2016; **16**: 6584-6591.
- [55] Zeng TS, Zhu W and Sheng D. Tuning topological phase and quantum anomalous Hall effect by interaction in quadratic band touching systems. *npj Quan Mater* 2018; **3**: 1-7.
- [56] Osada T. Topological properties of τ -type organic conductors with a checkerboard lattice. *J Phys Soc Japan* 2019; **88**: 114707.
- [57] Zhang RX, Wu F and Sarma SD. Möbius insulator and higher-order topology in $\text{MnBi}_{2n}\text{Te}_{3n+1}$. *Phys Rev Lett* 2020; **124**: 136407.
- [58] Yu FH, Mu HM and Zhuo WZ *et al.* Elevating the magnetic exchange coupling in the compressed antiferromagnetic axion insulator candidate EuIn_2As_2 . *Phys Rev B* 2020; **102**: 180404.
- [59] Ge Z, Zou Q and Zhang H *et al.* Superconductivity on edge: Evidence of a one-dimensional superconducting channel at the edges of single-layer FeTeSe antiferromagnetic nanoribbons. *ACS Nano* 2020; **14**: 6539-6547.
- [60] Lu XF, Wang NZ and Wu H *et al.* Coexistence of superconductivity and antiferromagnetism in $(\text{Li}_{0.8}\text{Fe}_{0.2})\text{OHFeSe}$. *Nat Mater* 2015; **14**: 325-329.
- [61] Ren M, Yan Y and Niu X *et al.* Superconductivity across Lifshitz transition and anomalous insulating state in surface K-doped $(\text{Li}_{0.8}\text{Fe}_{0.2}\text{OH})\text{FeSe}$. *Sci Adv* 2017; **3**: e1603238.
- [62] Chen M, Chen W and Zhang Z *et al.* Effects of magnetic dopants in $(\text{Li}_{0.8}\text{M}_{0.2}\text{OH})\text{FeSe}$ (M=Fe, Mn, Co): density functional theory study using a band unfolding technique. *Phys Rev B* 2017; **96**: 245111.
- [63] Ezawa M. Strong and weak second-order topological insulators with hexagonal symmetry and z_3 index. *Phys Rev B* 2018; **97**: 241402.